HortScience 60(3):303–309. 2025. https://doi.org/10.21273/HORTSCI18327-24

Combining Hyperspectral Imaging and a Transparent Hydroponics Bed to Analyze Growth and Age Distribution Dynamics of Entire Root Systems in Leafy Vegetables under In Situ Production Conditions

Ziyi Jin
Graduate School of Bioresource and Bioenvironmental Sciences, Kyushu University, Fukuoka, 819-0395, Japan

Daisuke Yasutake
Faculty of Agriculture, Kyushu University, Fukuoka 819-0395, Japan; and IoP Co-Creation Center, Kochi University, Nankoku, 783-8502, Japan

Yuki Sago
Faculty of Agriculture, Yamaguchi University, Yamaguchi, 753-8515, Japan

Tadashige Iwao
IoP Co-Creation Center, Kochi University, Nankoku, 783-8502, Japan

Gaku Yokoyama and Tomoyoshi Hirota
Faculty of Agriculture, Kyushu University, Fukuoka, 819-0395, Japan

Keywords. nutrient film technique, nondestructive method, spectral reflectance, spinach

Abstract. **Existing methods of observing plant roots are often limited by their inability to monitor the physiological information of root system under actual agricultural conditions. To address this limitation, we developed a novel method that enables nonlaboratory monitoring of the growth characteristics of crop root systems. This study explored the application of hyperspectral imaging technology to analyze the dynamic growth and aging of root systems throughout the cultivation period, specifically focusing on spinach (*Spinacia oleracea* L., cv. Wase Kurone Horenso) roots in a transparent hydroponics bed in a nutrient film technique (NFT) system. Root systems of spinach grown in the transparent bed were observed daily using a hyperspectral camera. An optimal index for the classification of root ages (days after emergence) was determined as the ratio of reflectance at 498 and 601 nm. Additionally, the distribution of root age was visualized over the entire cultivation period and showed the daily dynamics of root growth and aging. This study is useful for analyzing not only the growth but also the proportion of roots at different ages in the entire root system. This deepens our understanding of root development in soilless farming environments and provides an efficient, nondestructive technique for evaluating root vitality and developmental patterns.**

Roots are a main organ and account for an impressive 20% to as much as 80% of the total dry weight biomass of the plant body (Qi et al. 2019). They also play essential roles in the uptake of nutrients and water and in the storage of photosynthetic products (Neumann et al. 2009). Given the eco-physiological importance of roots, the observation and analysis of root growth characteristics are critical, especially for efficient crop production such as smart and precision agriculture.

Root growth characteristics such as "root age," which can be defined as the days after root emergence, greatly influence the vitality of roots and their essential roles mentioned above (Vetterlein and Doussan 2016). It is known that root growth leads to a developmental gradient from the tip to its base, with the tissues and structures changing over time. Because the root system is an aggregate of individual roots, it should have a spatial distribution of age that changes with time. Analyzing the spatial and temporal distributions of age in the root system can help us understand the dynamic characteristics of not only growth and/or senescence rates but also the vitality of the root system. Mainstream methods of the nondestructive determination of root age involve real-time tracking of roots (Vetterlein et al. 2016) or visual observation of their color change (Wells and Eissenstat 2001). These methods are either labor-intensive or subjective; therefore, a more labor-saving and objective approach to evaluating root age is necessary.

Hyperspectral imaging (HSI) is a labor-saving and objective approach to analyzing plant physiological information nondestructively and is based on the energy of light at specific wavelengths reflected according to plant structural and biochemical properties. This reflection occurs as light interacts with the electronic and molecular structures within the plant, creating distinct spectral signatures (ElMasry et al. 2010). Because HSI can collect spectral reflectance with narrow band intervals (1–5 nm), it provides a higher resolution of spectral information compared with that provided by other spectral imaging techniques. This makes it particularly suitable for investigations without prior information regarding which reflectance characteristics would change over a wide range of wavelengths. Often HSI is applied in preliminary investigations of the spectral characteristics of objects, and many studies have widely used HSI for the analysis of entire aboveground pants of plant to detect leaf and fruit diseases (Rumpf et al. 2010), assess nitrogen and water stresses in leaves (Tilling et al. 2007), and estimate leaf and stem biomass (Li et al. 2020). Furthermore, such HSI studies have also extracted eco-physiological information at the scale of all aboveground parts (Humplík et al. 2015). Although the application of HSI to root analyses has been limited to only a few studies, they demonstrated that HSI can provide physiological information about roots, similar to its use for the aboveground parts of plants. Therefore, HSI also has potential in root analyses, and it is expected that more related studies will emerge (Pierret 2008; Rewald and Meinen 2013).

Nakaji et al. (2008) conducted pioneering work using HSI technology to distinguish among new, senescent, and dead roots of tree species (poplar) in a rhizobox setup, which is known as traditional equipment for observing a part of the root system in the soil (Neufeld et al. 1989; Silva and Beeson 2011). This marked an important step toward realizing the potential of HSI in root analyses by offering a nondestructive approach to assess root physiological information. Building on this foundation, Bodner et al. (2018) used HSI to analyze the aging process of crop (barley) roots in a rhizobox setup. However, the rhizobox can be used only under specific experimental conditions and is not capable of allowing observations of growing crops under field natural conditions at agricultural production sites. However, Svane et al. (2019) opened new avenues for in situ root analyses by using HSI with minirhizotrons installed in a barley field. Although minirhizotrons are applicable at production field sites beyond the laboratory, they also can be used to observe only a part of the root system because of the opacity of soil (Villordon et al. 2011). The root system is composed of primary and lateral roots that become increasingly complex as they grow (Waidmann et al. 2020) and exhibit a spatial age distribution attributable to the aggregate of individual roots, as mentioned. Therefore, observing only a part of the root system cannot provide representative information of the entire root system or infer the age distribution. The observation scale of roots should cover the entire root

system, corresponding to the scale focused on by studies of the aboveground parts (Humplík et al. 2015).

To observe the entire root system, Le Marié et al. (2014) examined the application of HSI under a simplified growth condition (paper-based system); however, it was quite different from the agricultural production conditions (Krzyzaniak et al. 2021; Taylor et al. 1990). Overall, the application of HSI technology for entire root system analyses under agricultural production conditions remains underexplored, making it difficult to conduct comprehensive in situ root system analyses. However, the nutrient film technique (NFT) is a commonly used hydroponic system for leafy vegetables production. By replacing its cultivation bed with transparent materials, NFT may offer a novel approach for in situ analyses based on the nondestructive observation of the entire root system.

In the present study, we combined HSI and an NFT cultivation system with a transparent bed to nondestructively observe the entire root system of leafy vegetable during cultivation from planting to harvesting and analyzed the spatial and temporal distributions of root growth and root age. Spinach was used as the plant material because it is one of the most promising leafy vegetables for hydroponics (Sharma et al. 2018). A remarkable advantage of this study is the ability to focus on the entire root system rather than a part of it under in situ production conditions.

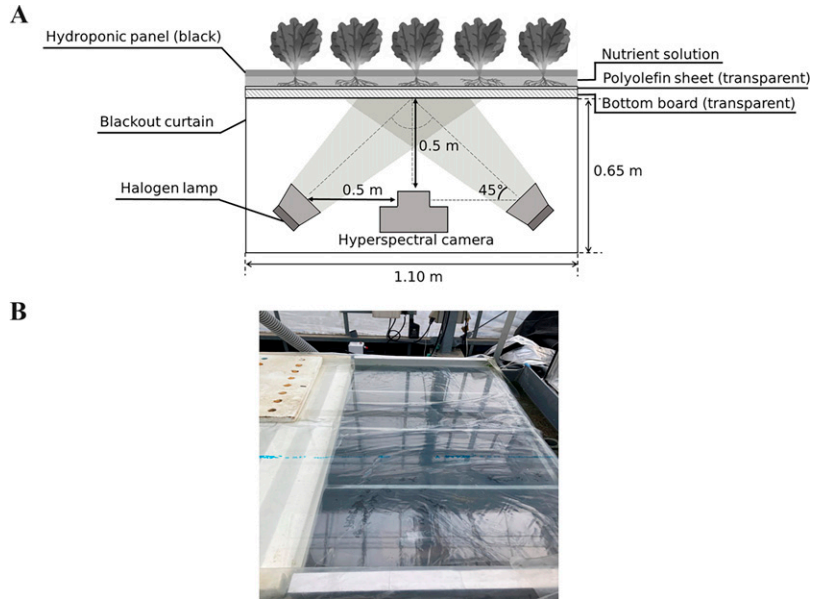

Fig. 1. Schematic diagram (**A**) of the spectral reflectance measurement of roots using a hyperspectral camera on part of the nutrient film technique (NFT) hydroponic bed comprising a hydroponic panel (underside painted black), transparent polyolefin sheet, and transparent acryl board. A top-down photograph (**B**) of the transparent hydroponic bed without the hydroponic panel. The nutrient solution flowed between the hydroponic panel and the polyolefin sheet. The hyperspectral camera and two halogen lamps were positioned beneath the NFT bed, which was enveloped with a blackout curtain.

Material and Methods

Equipment for observing roots. An NFT cultivation bed (15.0 m × 1.3 m) was used in a greenhouse located at the Ito Plant Experimental Fields and Facilities, Faculty of Agriculture, Kyushu University (Fig. 1). A part of the NFT cultivation bed (1.1 m × 1.3 m) had a transparent polyolefin sheet (thickness, 0.2 mm) and a transparent acrylic board (thickness, 70 mm) to observe the entire root system. The space (1.10 m × 1.30 m × 0.65 m) below this part of the bed was constructed to allow installation of a hyperspectral camera (Specim IQ; Specim Ltd., Oulu, Finland) and two halogen lamps (50 W) (JDR Φ50; Phoenix Electric Co., Ltd., Himeji, Hyogo, Japan). The camera lens was positioned 0.5 m below the bottom board of the NFT cultivation bed, and the bottom board was aligned perpendicular to the camera. The undersides of the hydroponic panels (0.85 m × 0.60 m) were painted black to facilitate easy differentiation of the roots from the background. The blackout curtain was spread beneath this space and remained closed at all times except during image acquisition to ensure that the roots were shielded from sunlight exposure.

Plant material and cultivation conditions. Seeds of spinach (*Spinacia oleracea* L., cv. Wase Kurone Horenso) were sown in urethane cubes (25 × 25 × 30 mm^3) at a rate of three seeds per cube and then grown with a sufficient water supply for 10 d. After germination, eight plant cubes with three healthy seedlings (plant height, approximately 20–30 mm) were selected and transplanted into hydroponic panels on the observation area of the NFT cultivation bed with a density of 88.9 plants/m^2. The plants were grown for 40 d, from 6 Nov to 16 Dec 2022, with a nutrient solution (Otsuka Agri Techno Co. Ltd., Japan) at an electrical conductivity of 2.0 $dS{\cdot}m^{-1}$ and a pH of 6.0. The root zone temperature was maintained within a range of 20 °C ± 1 °C. The nutrient solution contained 3.9 $mmol{\cdot}L^{-1}$ Ca^{2+}, 17 $mmol{\cdot}L^{-1}$ NO_3^-, 8.4 $mmol{\cdot}L^{-1}$ K^+, 1.6 $mmol{\cdot}L^{-1}$ SO_4^{2-}, 1.1 $mmol{\cdot}L^{-1}$ PO_4^{3-}, and 1.5 $mmol{\cdot}L^{-1}$ Mg^{2+}. The following environmental control systems in the greenhouse were used: roof and side-wall window ventilation occurred when the air temperature exceeded 22 °C, and heating with a heater (HK2027TEV; NEPON Inc., Tokyo, Japan) occurred when the air temperature dropped below 8 °C.

Image acquisition. The hyperspectral camera used to acquire spectral reflectance images can record the spectral reflectance (400–1000 nm) for each pixel. The resolution of the camera sensor was 512 × 512 pixels and the spectral resolution of the imaging system was approximately 3 nm (204 bands between 400 and 1000 nm). Because of the reduced sensitivity of the detector chip at its edge bands, which leads to spectra with a high level of noise, spectral bands of 420 to 950 nm were used in this study.

Before image acquisition, the integration time of the camera was calibrated to the background color to enhance the image quality. The integration time was adjusted based on empirical evidence until the cumulative highest spectral value across all pixels reached approximately 80% of the predetermined threshold value, as calculated using the Specim camera system. Exceeding this threshold can result in data loss during the image acquisition phase, whereas too short of an integration time may not leverage the full capabilities of the camera. We used an integration time of 1100 µs. Each acquired image was preprocessed using the standard normal variate (SNV) (Barnes et al. 1989).

We prepared two regions of 14 × 25 cm for plants on the hydroponic panels: region 1 was used for developing a model of root age classification and region 2 was used for application of the model to visualize the spatial and temporal distributions of root growth and root age. The respective regions included four plants. Region 1 was divided into four sub-regions (A, B, C, and D), each of which had 130 × 180 pixels and contained one plant. The image acquisition for each region was conducted daily from 6 Nov to 16 Dec 2022. A white reference panel was positioned in the middle between the polyolefin sheet and acryl board of the image acquisition

Received for publication 20 Nov 2024. Accepted for publication 30 Dec 2024.
Published online 4 Feb 2025.
This study was financially supported by Grants-in-Aid for Scientific Research (JSPS KAKENHI; Grant Nos. JP21H02318 and JP24K01882) from the Japan Society for Promotion of Science, and the Cabinet Office grant in aid, Evolution to Society 5.0 Agriculture Driven by Internet of Plants (IoP), Japan. We would like to thank Editage (www.editage.jp) for English language editing.
D.Y. is the corresponding author. E-mail: yasutake@bpes.kyushu-u.ac.jp.

Fig. 2. Schematic diagram of the method of tracking root age continuously over 3 d (days 1, 2, and 3). To easily detect roots, the images were expressed as white for roots and black for others. The present study defined the root segment located approximately 1 cm from the root tip as "1 day old," and root age increased accordingly as time progressed (i.e., 1 d old on day 1 changed to 2 d old on day 2). At the same time, new 1-d-old-root segment appeared on the same root on day 2. These root segments continue to age on day 3.

system and imaged simultaneously during each image acquisition to compensate for the light transmission path through the acrylic board.

Root age definition and selection of root segment for age classification. Because the structure of the root tip is fairly different from the maturation parts of roots, this study avoided sampling the root tip. Mature roots are characterized by the presence of numerous root hairs; however, the number of root hairs in hydroponically grown roots is minimal (Ahn et al. 2004) and difficult to detect at the resolution of the images captured in this study. Therefore, the segment (length, 2 mm) of the root approximately 1 cm away from the root tip was classified as 1-d-old root in this study, and the age of this root segment increased with the number of cultivation days. If a segment of the root appeared on the second day of cultivation, then its age would be 1 d on the second day, and it increased to 2 d on the third day of cultivation (Fig. 2). We focused on one easily observable root from each sub-region and tracked two segments along the same root to capture spatial and temporal changes of root age. For all of the sub-regions, eight root segments (A1, A2, B1, B2, C1, C2, D1, and D2) were selected, and their coordinates were as follows: segment A1 (72, 96); segment A2 (54, 81); segment B1 (97, 128); segment B2 (89, 115); segment C1 (25, 125); segment C2 (37, 142); segment D1 (94, 53); and segment D2 (83, 37) (Fig. 3). Each root segment was tracked over an extended period to develop a model of root age classification: segment A1 from 1 to 14 d; segment A2 from 1 to 19 d; segment B1 from 1 to 15 d; segment B2 from 1 to 15 d; segment C1 from 1 to 21 d; segment C2 from 1 to 18 d; segment D1 from 1 to 25 d; and segment D2 from 1 to 28 d. Although root positions for each segment were generally stable, minor displacements occasionally occurred because of water flow, in which case the coordinates were manually adjusted. For each root segment, 10 pixels were extracted from the hyperspectral images, and their average reflectance was calculated to represent the spectral reflectance of each segment.

Root spectral characteristics capture and image analysis. To classify the roots into different ages in region 1, we determined the optimal index as a ratio of reflectance at two wavelengths. We calculated ratios for a range of 420 to 950 nm and conducted a correlation analysis with root age. We assumed that the relationship between the ratio and root age is

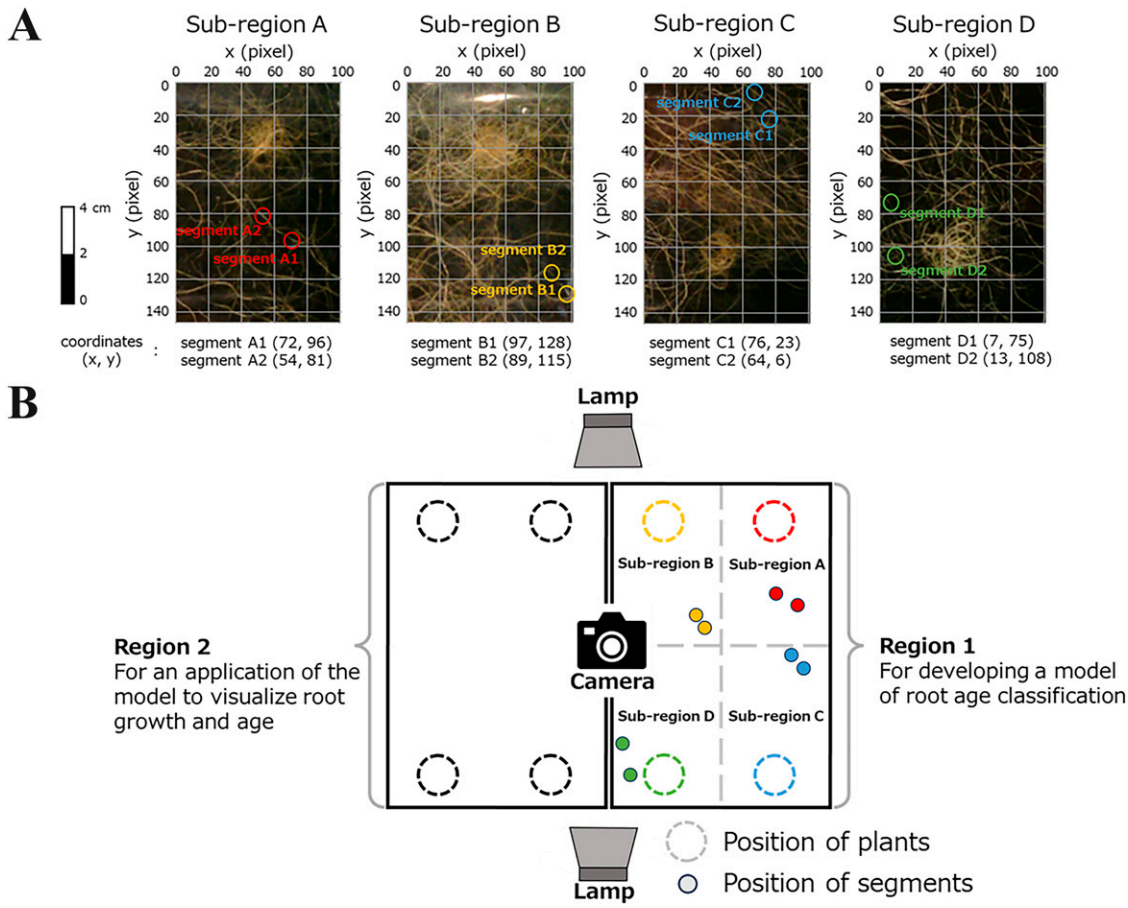

Fig. 3. Red green blue (RGB) images (**A**) of the tracked root segment for sub-regions A, B, C, and D with one plant and a schematic diagram (**B**) of the positions of each region, plant, segment, lamps, and camera. A single root that was easy to observe was selected for each region, and two root segments along the same root were determined. Their coordinates are shown below the respective images. These segments were tracked daily based on the coordinates that were slightly adjusted when minor displacement occurred because of water flow.

monotonic and not limited to only linearity. Therefore, we used Spearman's correlation coefficient, which can evaluate both linear and nonlinear monotonic relationships, instead of Pearson's correlation coefficient, which is better suited for assessing linear relationships. The performance of the reflectance ratio when representing root age was evaluated using the absolute value of the Spearman's correlation coefficient (|ρ|). The ratio with the largest |ρ| was selected as the optimal index for analyzing root age. All statistical analyses in this study were conducted using Python (version 3.9) with the libraries of pandas (version 1.5.3) and numpy (version 1.24.3).

To visualize the spatial and temporal distributions of the growth and age of the entire root system in region 2, we applied the analysis methodology with the optimal index to the region in the daily acquired root images. Different false colors were assigned to represent roots at different ages, and the daily changes for each age of the roots were evaluated.

Results and Discussion

Spectral reflectance of different ages in each root segment. Figure 4 shows the spectral reflectance for each root segment (A1, A2, B1, B2, C1, C2, D1, and D2) 14 d after emergence under the growing conditions of the present study. A similar pattern in the reflectance among all segments was observed, although the reflectance of segments D1 and D2 were relatively higher than that of the others across the entire wavelength range. This higher reflectance in segments D1 and D2 may be attributable to the halogen lamps, which may not illuminate every position within the acquisition area evenly, and segments D1 and D2 may have received more light because they were physically closer to the lamps than the others were. This nonuniform lighting often occurs in the capture of hyperspectral images (Rinnan et al. 2009), particularly outside of laboratory conditions, as in the present study. The nonuniform lighting usually causes overestimation or underestimation of the reflectance of the observed object. However, because the spectral reflectance of segment D1 and that of D2 had patterns similar to those of the other segments, we considered them as useable measurements. For each segment, the daily reflectance changes were not affected by the nonuniform lighting because of the fixed point measurement. However, when analyzing all segments together, the overestimation or underestimation of reflectance would cause some errors in the analysis. Therefore, we used SNV as a preprocessing method to eliminate the errors caused by nonuniform lighting conditions. Furthermore, because this study used the ratio of reflectance at two wavelengths to classify root age, the errors were mitigated to some extent. To ensure the versatility of the proposed methodology across various lighting conditions even in different cultivation environments, we preserved the data of segments D1 and D2 to determine the optimal index of root age.

The reflectance of each root exhibited a deep trough at approximately 680 nm. This suggests that light at approximately 680 nm was likely absorbed by the roots and/or the nutrient solution. Because this wavelength range is also the primary absorption range of chlorophyll, a certain amount of chlorophyll may be present in the roots. Roots can produce small amounts of chlorophyll when continuously exposed to light (Kobayashi et al. 2013). The presence of chlorophyll in the roots may be caused by the translucency of the hydroponic panel, which was made of polyethylene foam. Although the panel appeared opaque to the naked eye, a small amount of light still penetrated the panel and illuminated the roots under daytime sunlight, which resulted in exposure of the roots to trace amounts of sunlight, potentially leading to chlorophyll production. Additionally, the production of algae in the nutrient solution could have been a reason for the troughs at approximately 680 nm. Although the reflectance at approximately 900 nm was still somewhat noisy, we retained these data to ensure spectral completeness as much as possible.

Figure 5 shows the spectral reflectance of the eight root segments on different days after the emergence of the roots (different ages). The observation period for sgements D1 and D2 were longer than that of the other six segments; therefore, their spectral reflectance included additional lines. Within each segment, 1-d-old roots exhibited features that were both similar to and different from those of older roots. The 1-d-old roots of segments B1 and C1 showed overall lower reflectance, whereas segment B2 displayed higher reflectance in the range of 420 to 650 nm. The different manners of reflectance observed in some 1-d-old roots (e.g., segments B1 and C1) were consistent with those reported by Nakaji et al. (2008). The 1-d-old roots may belong to the elongation part of roots, which is located between the root tip and maturation part, and have a structure similar to that of the maturation part (Waisel et al. 2002). However, it may still lead to different reflectance compared with that of the maturation part. Except for the 1-d-old roots in segments B1 and C1, the reflectance in the range of 420 to 800 nm decreased with increasing root age. Nakaji et al. (2008) showed that as roots aged, the reflectance in the range of 700 to 1000 nm first increased and then became stable in older roots; however, the change in the range of 800 to 950 nm with age was irregular in this study. The reason for the low reflectance in 1-d-old roots in segments B1 and C1 could be that the diameter of newly grown roots is smaller than that of mature roots, resulting in greater transparency. This allowed more incident light to pass through the 1-d-old roots and become absorbed by the black background of the panel, leading to a reduction in root reflectance. The troughs at 680 nm became clearer with increasing root age, particularly in segments A2 and D2. This may have been caused by the gradual increase in the chlorophyll content within the roots as they aged. The decrease in reflectance in the wavelength range of 420 to 800 nm with age may be caused by lignification of the roots. Lignin, produced by lignification, has strong absorption bands in the ultraviolet and visible light domains, has the highest absorption at 440 nm, and shows a gradual decrease in absorption up to 800 nm (Skulcova et al. 2017). As the roots age, the content of lignin produced by lignification should increase, leading to greater absorption of light in the range of 420 to 800 nm and, consequently, a reduction in root reflectance within this range.

Selection of the optimal index. Figure 6 shows the absolute values of the Spearman correlation coefficients, which were calculated between the days after root emergence and the root reflectance ratio for each wavelength pair ($R_{\lambda a}/R_{\lambda b}$). The upper left and lower right parts of the image were symmetrical. Three areas with a relatively high correlation were

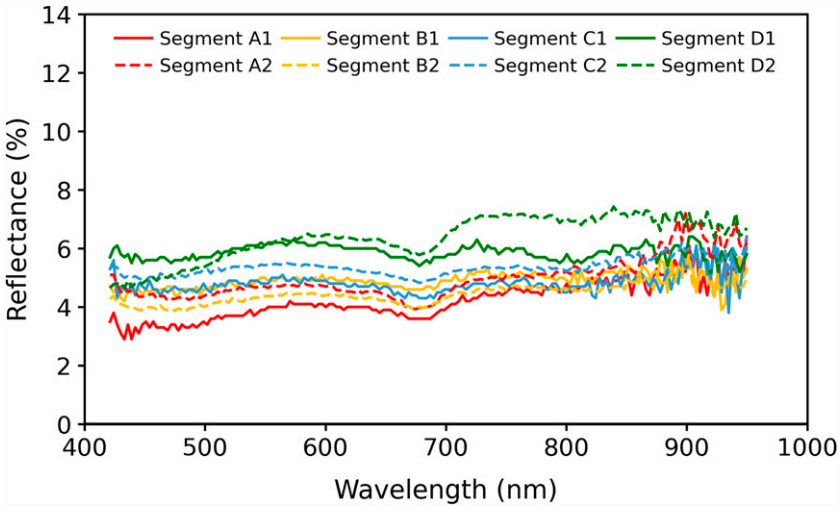

Fig. 4. Spectral reflectance of spinach roots on the day 14 after emergence for each root segment (A1, A2, B1, B2, C1, C2, D1, and D2 shown in Fig. 3). The solid line indicates root segments A1, B1, C1, and D1, and the dotted line indicates root segments A2, B2, C2, and D2. The reflectance values were averaged for 10 pixels of each segment.

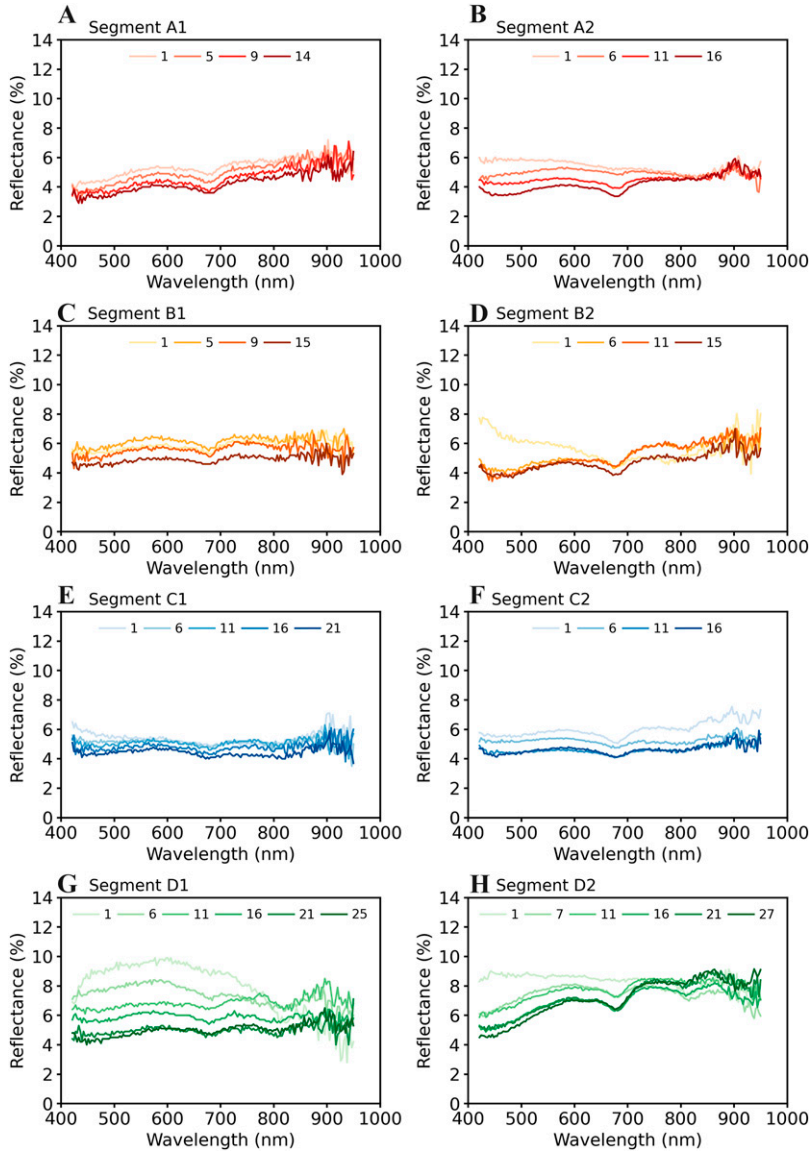

Fig. 5. Hyperspectral reflectance of spinach roots for each root segment (**A**, segment A1; **B**, segment A2; **C**, segment B1; **D**, segment B2; **E**, segment C1; **F**, segment C2; **G**, segment D1; **H**, segment D2) on different days after emergence. The reflectance values were averaged for 10 pixels of each segment. The values of explanatory note implied the days after the emergence of roots.

present in the lower right area of the matrix, corresponding to areas of approximately $R_{500–660}/R_{420–550}$, $R_{700–950}/R_{420–550}$, and $R_{700–900}/R_{690–720}$. However, areas of approximately $R_{550–690}/R_{550–690}$ and $R_{750–950}/R_{750–950}$ showed a lower correlation. Based on these results, we selected the ratio (R_{601}/R_{498}) with the highest Spearman's correlation coefficient ($|\rho| = 0.82$) as the optimal index, which was similar to the wavelengths of 480 nm and 609 nm used by Nakaji et al. (2008). Other ratios, such as R_{553}/R_{461} ($\rho = 0.74$) and R_{513}/R_{472} ($\rho = 0.71$), also exhibited high correlations and shared similarities with the wavelengths used by Nakaji et al. (2008). These wavelengths indicate the potential applicability of multiple ratios for root age classification. Wavelengths of 498 nm and 601 nm are both in the visible light range, suggesting that it may be possible to classify root age by using visible light multispectral imaging as a cost-effective method. In the present study, the classification of root age should not depend on the chlorophyll content within the roots or the presence of attached algae for the following reasons. First, although lower reflectance at each root segment was observed at one of the primary absorption wavelengths of chlorophyll, 680 nm (Fig. 5), the correlation between root age and the reflectance ratio was not strong at this wavelength (Fig. 6). This might be attributable to differences in the amount of sunlight received at each segment, as influenced by the greenhouse structure or the arrangement of aboveground leaves, resulting in spatial variations in chlorophyll contents among root segments. Another major chlorophyll absorption wavelength, 450 nm, showed a high correlation with the reflectance ratio at other wavelengths. However, no distinct trough was observed at 450 nm; therefore, it was not possible to determine whether the high correlation at 450 nm was related to chlorophyll (Fig. 5). Therefore, we can conclude that the wavelengths chosen for root age classification in this study were not predominantly influenced by the chlorophyll content.

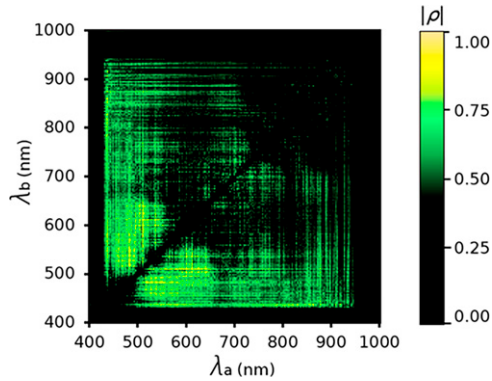

Fig. 6. Matrix of the absolute value of the Spearman correlation coefficient ($|\rho|$) between the days after root emergence and the ratio of root reflectance for each pair of wavelengths ($R_{\lambda a}/R_{\lambda b}$), where $R_{\lambda a}$ and $R_{\lambda b}$ represent the reflectance values at wavelengths of λ_a and λ_b, respectively. The color bar illustrates the correlation strength, where brighter colors denote higher Spearman's correlation coefficients.

Additionally, the high correlation area mentioned in our study corresponded to more than half of the wavelength combinations for classifying roots of different ages, which were based on the Jeffries–Matusita distance derived by Nakaji et al. (2008). Although different types of roots were selected as the study material for the present study and that of Nakaji et al. (2008), the common characteristics of the reflectance at these wavelengths may be the same as their ages change.

Figure 7 shows the relationship between days after emergence and the reflectance ratio of 498 to 601 nm for root segments A1, A2, B1, B2, C1, C2, D1, and D2 with a linear regression line (the orange area depicts the 95% confidence interval and the gray area depicts the 95% prediction interval). Overall, the days after emergence were directly proportional to the ratio (R_{601}/R_{498}), with a Spearman's correlation coefficient of 0.82 ($P = 1.68 \times 10^{-6}$), indicating that the data obtained even under nonuniform lighting conditions were reasonable for analyses. Estimating the root age based on the relationship between the date after emergence and index could suggest an error margin of approximately 3 d, as determined by the 95% prediction interval.

Visualization of root age. Figure 8A shows false color images of roots of different ages

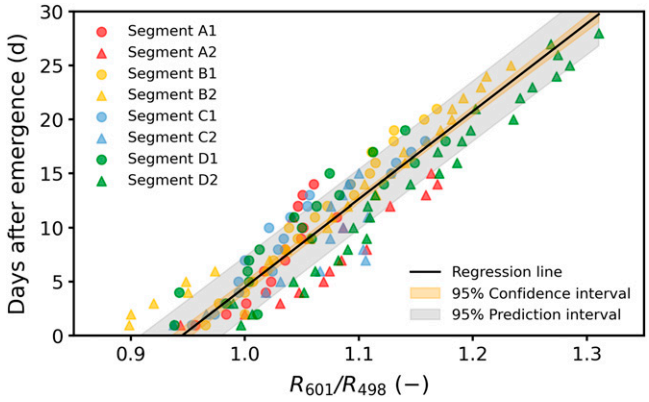

Fig. 7. Relationship between days after emergence as root age and the ratio of R_{601} and R_{498} (R_{601}/R_{498}) for root segments A1, A2, B1, B2, C1, C2, D1, and D2, with a linear regression line and a gray area depicting the 95% confidence interval. R_{601} and R_{498} represent the reflectance values at wavelengths of 601 nm and 498 nm, respectively.

(days after emergence) at 10, 20, 30, 40, and 50 days after sowing (DAS) in region 2. We classified the roots into the following four stages, 0 to 5 d, 6 to 15 d, 16 to 28 d, and 29 d of age or older, according to the optimal index (R_{601}/R_{498}) determined based on Fig. 5. Because we did not obtain information about roots older than 29 d in all segments, we regarded all roots with an optimal index greater than that of day 28 in Fig. 6 as being older than 29 d. The roots grew from the base of the plants and gradually expanded into the surrounding areas over time. As DAS increased, the emergence of older roots was observed at the base of the plants, leading to the roots from stages 4 to 1 being arranged in a sequence from the base of the plant toward the outer area at 50 DAS. Consequently, the changes in quantity and age with root growth were visualized using false color image analysis. The appearance of roots at stage 4 (older than 29 d) at 30 DAS was anomalous considering the timeframe because it remained at stage 2 (6–15 d) 10 d before 30 DAS (20 DAS). This may be attributed to errors in classifying the age of the roots (Fig. 6).

Figure 8B shows the daily change in the percentage of the area occupied by the entire root system and each growth stage within region 2 from 10 to 50 DAS. The percentage of the entire root system area remained low and stable from 10 DAS, began to increase rapidly from 19 to 31 DAS, slowed after 32 DAS, and finally reached 96% at 50 DAS. Growth stagnation of roots before 18 DAS and rapid root growth beginning at 19 DAS are both considered natural responses of hydroponically grown spinach (Smolders et al. 1991). On 32 DAS, the root area occupied almost the entirety of region 2, leading to considerable root overlap. This suggests that root growth cannot be accurately analyzed solely based on the area of the entire root system during this phase.

The stage 1 area in region 2 increased slowly from 10 to 20 DAS, began to accelerate from 21 DAS, and then shifted toward a decrease from 32 DAS onward. The stage 2 areas grew slowly from 10 to 27 DAS, remained stable between 28 and 40 DAS, and decreased slowly after 41 DAS. Stages 3 and 4 areas began to appear in small amounts beginning at 18 and 26 DAS, respectively, with both areas slowly and continuously increasing. Among all root stages, only those at stages 1 and 2 exhibited a decreasing trend, which emerged at 29 and 41 DAS, respectively. Although new roots tend to grow at the bottom of the NFT (Graves 1983), roots at stages 1 and 2 continued to decrease after 29 and 41 DAS for two possible reasons. Using stage 1 as an example, the first possibility was that after 29 DAS, the rate of new root emergence may be lower than that of aged roots (the rate of stage 1 roots transitioning to stage 2); however, the cause of this difference in emerging and aging rates was not clear. The second possibility was that as the roots grow, new roots may start to emerge outside region 2. This left the existing stage 1 roots within region 2 to gradually age and transform into stage 2 roots, leading to a reduced percentage of the stage 1 root area in region 2 after 29 DAS. The same reasoning applies to stage 2 roots, explaining their decrease after 41 DAS. Nakaji et al. (2008) also showed the distribution of root age at different DAS, but they only visualized the age of a small part of roots for 3 d. In contrast, we visualized the spatial and temporal distributions of age of the entire root system for 50 d after planting (Fig. 7B). This approach may provide a deeper understanding of root growth in relation to age dynamics.

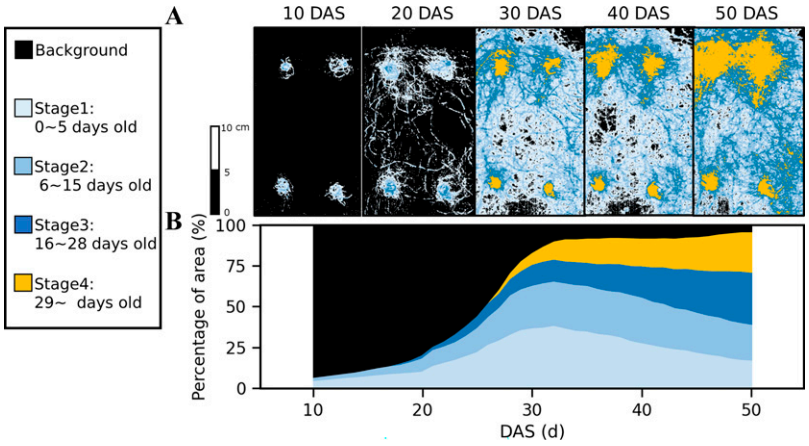

Fig. 8. False color images of roots located in region 2 at various stages: 10, 20, 30, 40, and 50 d after sowing (DAS) (**A**) and the daily change in the percentage of the area occupied by each growth stage of the root system within region 2 from 10 to 50 DAS (**B**).

Conclusions

This study demonstrated the effective application of HSI technology for monitoring the physiological and ecological characteristics of spinach roots in hydroponic cultivation. Using a hyperspectral camera, this study achieved detailed observations of root growth, and the development of an optimal index based on the ratio of reflectance at two wavelengths (R_{601}/R_{498}) enabled the classification of root age. We conducted daily visualization of the age distribution of the root system throughout the entire period from planting to harvest. This study marks the pioneering application of a visualization method for root age distribution using HSI technology on a transparent hydroponics bed in an NFT system. Because the NFT system is widely used in agricultural production, the results represent the first instance of a nondestructive approach to categorizing root age of crop plants outside of laboratory conditions. This approach not only enhances our understanding of root development in soilless cultivation systems but also offers a high throughput, nondestructive method of assessing root health and growth dynamics.

When comparing this study with that of Nakaji et al. (2008), which used a different plant species, we found that similar wavelengths were used for root age classification. This suggests that these wavelengths may have general applicability across different plant species. However, this study still had some limitations. Because only spinach was used as the plant material, the optimal index derived can only ensure high accuracy for the root age classification of this particular species. Additionally, this study was conducted under only one environmental condition. If the cultivation environment changes (such as

root zone temperature, nutrient concentration, and others), then the growth rate of the roots would also change, and this may cause a decrease in the accuracy of the root age analysis. Therefore, further research is necessary to verify the applicability of the optimal index to other species and different environments.

Despite these limitations, the findings of this study could contribute to improving the precision and efficiency of agricultural production, particularly in controlled environments such as plant factories where hydroponic systems are prevalent, thereby facilitating informed decision-making in crop management.

References Cited

Ahn SJ, Shin DP, Schachtman R. 2004. Expression of KT/KUP genes in arabidopsis and the role of root hairs in K^+ uptake. Plant Physiol. 134(3):1135–1145. https://doi.org/10.1104/pp.103.034660.

Barnes RJ, Dhanoa SJ, Lister MS. 1989. Standard normal variate transformation and de-trending of near-infrared diffuse reflectance spectra. Appl Spectrosc. 43(5):772–777. https://doi.org/10.1366/0003702894202201.

Bodner G, Nakhforoosh T, Arnold D, Leitner A. 2018. Hyperspectral imaging: A novel approach for plant root phenotyping. Plant Methods. 14:84. https://doi.org/10.1186/s13007-018-0352-1.

ElMasry G, Sun DW, Sun DW. 2010. Principles of hyperspectral imaging technology, p 3–43. Hyperspectral imaging for food quality analysis and control. Elsevier, Amsterdam. https://doi.org/10.1016/B978-0-12-374753-2.10001-2.

Graves CJ. 1983. The nutrient film technique, p 1–44. In: Janick J (ed). Horticultural reviews. Wiley Press, New York, NY, USA. https://doi.org/10.1002/9781119750802.

Humplík JF, Lazár A, Husičková L, Spíchal D. 2015. Automated phenotyping of plant shoots using imaging methods for analysis of plant stress responses – a review. Plant Methods. 11:29. https://doi.org/10.1186/s13007-015-0072-8.

Kobayashi K, Sasaki K, Noguchi D, Fujinuma H, Komatsu M, Kobayashi M, Sato K, Toyooka K, Sugimoto KK, Niyogi H, Wada T, Masuda D. 2013. Photosynthesis of root chloroplasts developed in Arabidopsis lines overexpressing GOLDEN2-LIKE transcription factors. Plant Cell Physiol. 54(8):1365–1377. https://doi.org/10.1093/pcp/pct086.

Krzyzaniak Y, Cointault C, Loupiac E, Bernaud F, Ott C, Salon A, Laybros S, Han MC, Héloir M, Adrian S, Trouvelot F. 2021. In situ phenotyping of grapevine root system architecture by 2D or 3D imaging: Advantages and limits of three cultivation methods. Front Plant Sci. 12:638688–638688. https://doi.org/10.3389/fpls.2021.638688.

Le Marié C, Kirchgessner D, Marschall A, Walter A, Hund N. 2014. Rhizoslides: Paper-based growth system for non-destructive, high throughput phenotyping of root development by means of image analysis. Plant Methods. 10(1):13. https://doi.org/10.1186/1746-4811-10-13.

Li B, Xu L, Zhang J, Han C, Bian G, Li J, Liu L, Jin M. 2020. Above-ground biomass estimation and yield prediction in potato by using UAV-based RGB and hyperspectral imaging. ISPRS J Photogramm Remote Sens. 162:161–172. https://doi.org/10.1016/j.isprsjprs.2020.02.013.

Nakaji T, Noguchi H, Oguma K. 2008. Classification of rhizosphere components using visible–near infrared spectral images. Plant Soil. 310(1-2):245–261. https://doi.org/10.1007/s11104-007-9478-z.

Neufeld HS, Durall PM, Rich DT, Tingey DM. 1989. A rootbox for quantitative observations on intact entire root systems. Plant Soil. 117(2):295–298. https://doi.org/10.1007/BF02220725.

Neumann G, George C, Plassard TS. 2009. Strategies and methods for studying the rhizosphere—the plant science toolbox. Plant Soil. 321(1–2):431–456. https://doi.org/10.1007/s11104-009-9953-9.

Pierret A. 2008. Multi-spectral imaging of rhizobox systems: New perspectives for the observation and discrimination of rhizosphere components. Plant Soil. 310(1–2):263–268. https://doi.org/10.1007/s11104-008-9651-z.

Qi Y, Wei C, Chen L, Chen W. 2019. Plant root-shoot biomass allocation over diverse biomes: A global synthesis. Glob Ecol Conserv. 18:e00606. https://doi.org/10.1016/j.gecco.2019.e00606.

Rewald B, Meinen C. 2013. Plant roots and spectroscopic methods – analyzing species, biomass, and vitality. Front Plant Sci. 4:393. https://doi.org/10.3389/fpls.2013.00393.

Rinnan Å, van den Berg F, Balling Engelsenn S. 2009. Review of the most common pre-processing techniques for near-infrared spectra. Trends Anal Chem. 28(10):1201–1222. https://doi.org/10.1016/j.trac.2009.07.007.

Rumpf T, Mahlein U, Steiner EC, Oerke HW, Dehne L, Plümer AK. 2010. Early detection and classification of plant diseases with support vector machines based on hyperspectral reflectance. Comput Electron Agric. 74(1):91–99. https://doi.org/10.1016/j.compag.2010.06.009.

Sharma N, Acharya S, Kumar K, Singh N, Chaurasia OP. 2018. Hydroponics as an advanced technique for vegetable production: An overview. J Soil Water Conserv. 17(4):364–371. https://doi.org/10.55627/zoobotanica.001.01.0630.

Silva DD, Beeson RC. 2011. A large-volume rhizotron for evaluating root growth under natural-like soil moisture conditions. HortScience. 46(12):1677–1682. https://doi.org/10.21273/HORTSCI.46.12.1677.

Skulcova A, Majova M, Kohutova M, Grosik J, Sima M, Jablonsky V. 2017. UV/Vis spectrometry as a quantification tool for lignin solubilized in deep eutectic solvents. BioRes. 12(3):6713–6722. https://doi.org/10.15376/biores.12.3.6713-6722.

Smolders E, Merckx F, Schoovaerts K, Vlassak R. 1991. Continuous shoot growth monitoring in hydroponics. Physiol Plant. 83(1):83–92. https://doi.org/10.1111/j.1399-3054.1991.tb01285.x.

Svane SF, Dam JM, Carstensen KT, Kristensen EB. 2019. A multispectral camera system for automated minirhizotron image analysis. Plant Soil. 441(1–2):657–672. https://doi.org/10.1007/s11104-019-04132-8.

Taylor HM, Upchurch BL, McMichael DR. 1990. Applications and limitations of rhizotrons and minirhizotrons for root studies. Plant Soil. 129(1):29–35. https://doi.org/10.1007/BF00011688.

Tilling AK, O'Leary JG, Ferwerda SD, Jones GJ, Fitzgerald D, Rodriguez R, Belford GJ. 2007. Remote sensing of nitrogen and water stress in wheat. Field Crops Res. 104(1–3):77–85. https://doi.org/10.1016/j.fcr.2007.03.023.

Vetterlein D, Doussan C. 2016. Root age distribution: How does it matter in plant processes? A focus on water uptake. Plant Soil. 407(1–2):145–160. https://doi.org/10.1007/s11104-016-2849-6.

Villordon A, LaBonte D, Solis J. 2011. Using a scanner-based minirhizotron system to characterize sweetpotato adventitious root development during the initial storage root bulking stage. HortScience. 46(3):513–517. https://doi.org/10.21273/HORTSCI.46.3.513.

Waidmann S, Sarkel J, Kleine-Vehn E. 2020. Same same, but different: Growth responses of primary and lateral roots. J Exp Bot. 71(8):2397–2411. https://doi.org/10.1093/jxb/eraa027.

Waisel Y, Eshel A, Kafkafi U. 2002. Plant roots – the hidden half (3rd ed). Marcel Dekker Inc., New York, NY, USA. https://doi.org/10.1201/9780203909423.

Wells CE, Eissenstat DM. 2001. Marked differences in survivorship among apple roots of different diameters. Ecology. 82(3):882–892. https://doi.org/10.2307/2680206.